SCIENTIFIC REPORTS

An Atomistic-Scale Study for Thermal Conductivity and Thermochemical Compatibility in (DyY)Zr$_2$O$_7$ Combining an Experimental Approach with Theoretical Calculation

Liu Qu[1], Kwang-Leong Choy[1] & Richard Wheatley[2]

Ceramic oxides that have high-temperature capabilities can be deposited on the superalloy components in aero engines and diesel engines to advance engine efficiency and reduce fuel consumption. This paper aims to study doping effects of Dy^{3+} and Y^{3+} on the thermodynamic properties of ZrO$_2$ synthesized via a sol-gel route for a better control of the stoichiometry, combined with molecular dynamics (MD) simulation for the calculation of theoretical properties. The thermal conductivity is investigated by the MD simulation and Clarke's model. This can improve the understanding of the microstructure and thermodynamic properties of (DyY)Zr$_2$O$_7$ (DYZ) at the atomistic level. The phonon-defect scattering and phonon-phonon scattering processes are investigated via the theoretical calculation, which provides an effective way to study thermal transport properties of ionic oxides. The measured and predicted thermal conductivity of DYZ is lower than that of 4 mol %Y$_2$O$_3$ stabilized ZrO$_2$ (4YSZ). It is discovered that DYZ is thermochemically compatible with Al$_2$O$_3$ at 1300 °C, whereas at 1350 °C DYZ reacts with Al$_2$O$_3$ forming a small amount of new phases.

High temperature ceramic materials such as 6–8 wt. % Y$_2$O$_3$ stabilized ZrO$_2$ (6–8 wt. % YSZ, i.e. 3–4.5 mol % YSZ) have been investigated and used in extremely severe environments such as the thermal barrier coatings (TBCs) on turbine blades[1]. 6–8 wt. % YSZ coatings deposited on turbine blades, can improve the application temperature and the performance of engines for propulsion in aviation, automotive and marine industries and power generative system[2,3]. The deposited ceramic TBCs on superalloy components can lower the surface temperature and increase the durability of the components, which advances the engine efficiency and brings about environmentally friendly effects such as low emission and fuel consumption. However, the phase instability and sintering effects of conventional 6–8 wt. % YSZ coatings above 1200 °C, which result in reduced durability and reliability, have hindered further application in TBCs[4].

Various ceramic materials are developed to satisfy the requirements of new TBCs including low thermal conductivity, high coefficient of thermal expansion (CTE), thermochemical stability, and sintering resistance[5,6]. Promising compositions such as Re$_2$Zr$_2$O$_7$, La$_2$Ce$_2$O$_7$, LaMgAl$_{11}$O$_{19}$, quasi-eutectoid (La$_{1-x}$Yb$_x$)$_2$Zr$_2$O$_7$, and Y$_4$Al$_2$O$_9$ which are reported to exhibit improved thermomechanical properties, are considered as potential candidates for new TBCs[7–11]. The nonstoichiometry pyrochlore Nd$_{2-x}$Zr$_{2+x}$O$_{7+x/2}$ shows better thermomechanical property than 4YSZ[12]. 5 to 20 mol % Dy$_2$O$_3$ doped 5YSZ has been investigated by Wang[13], who summarized that air-plasma-sprayed coatings exhibited the monoclinic and cubic structures and 10 mol % (Dy, Y)-ZrO$_2$ coatings had the highest resistance to heat transfer. It is reported that Dy-YSZ is composed of the cubic/tetragonal structure at lower doping level, and the thermal conductivity decreases with the addition of Dy$_2$O$_3$ and Y$_2$O$_3$ to ZrO$_2$[14].

[1]UCL Institute for Materials Discovery, University College London, London, WC1E 6BT, UK. [2]Department of Chemistry, University of Nottingham, Nottingham, NG7 2RD, UK. Correspondence and requests for materials should be addressed to K.-L.C. (email: k.choy@ucl.ac.uk)

However, there is a paucity of studies on the thermodynamic properties of the DYZ system at the atomistic level. Furthermore, the sol-gel approach is effective in controlling the chemical composition and particle morphology, in which case intrinsic material properties can be determined.

MD simulation can be performed to systematically predict the theoretical material properties of various chemical compositions[15]. It involves the calculation of the position and momentum of trajectories of particles based on Newton's second law of motion[16]. MD simulation enables nano-size models consisting of several million particles and microseconds of real-time to be studied, in contrast to various other modelling approaches[17]. Thermodynamic properties, such as transport properties and vibrational frequencies can be predicted from the time-dependent trajectories of atoms in an MD simulation system[18]. In the direct non-equilibrium MD simulation method, a perturbation is applied to the simulation cell, and the response of the system, such as the heat flux, is measured, from which basis thermal conductivity can be determined[19].

There is limited information on the thermodynamic properties of DYZ, while no reports exist on the MD simulation of DYZ. This paper emphasizes the development of novel ionic oxide materials via experiment and theoretical calculation. Doping ZrO_2 with Dy^{3+} which has a higher atomic weight and larger ionic radius than Zr^{4+} can potentially modify the thermal conductivity. The relationship between chemical composition, microstructure and thermal conductivity is studied. The phonon scattering processes which significantly influence the thermal conductivity are highlighted by the theoretical calculation based on the MD model and Clarke's model. We have investigated the thermochemical compatibility of DYZ with Al_2O_3 by the structural characterization and the local chemical environment study of powder mixtures. This present work improves the understanding of the microstructure and thermodynamic properties DYZ on the atomistic level.

Experimental

Processing Routes. The starting materials consist of metal salts of Y^{3+} and Dy^{3+}, 1-propanol, zirconium propoxide in 1-propanol and acetylacetone. These precursors were mixed to form a solution with the desired molar ratio under argon atmosphere to prevent the fast hydrolysis of $Zr(OPr)_4$ with H_2O. The molar ratio: $[AcAc]/[Zr(OPr)_4] = 0.7$. The concentration of $Zr(OPr)_4$ was 0.5 mol/L. Deionized water was added to the 1-propanol to achieve the concentration of 10 mol/L. The water in 1-propanol was mixed with the $Zr(OPr)_4$ solution with the molar ratio $[H_2O]/[Zr(OPr)_4] = 8.5$. The mixed solution was stirred mechanically for 30 min. The homogeneous sol was dried at 50 °C for several hours to obtain the gel, followed by calcination at 950 °C for 3 hours to obtain ceramic powders. The as-sintered powders were treated at 1200 °C for 2 hours, followed by uniaxial compaction of the powders into pellets. The pellets were sintered at 1200 °C for 6 hours.

Thermochemical Compatibility. The thermodynamic stability between the as-synthesized DYZ powders and Al_2O_3 was studied using a solid-state reaction method. The as-synthesized powders were mixed with Al_2O_3 in an equal mass ratio, followed by ball milling for 8 hours. The ball milled powders were sintered at 1300 °C and 1350 °C under air atmosphere to study the thermochemical compatibility.

Characterization. The crystal structure was characterized via X-ray diffraction (XRD) using a Siemens D500 X-ray diffractometer (Cu-Kα radiation, $\lambda = 1.54$ Å). Raman analysis was conducted via a Horiba Jobin-Yvon LabRAM spectrometer equipped with an Olympus BX41 microscope (He-Ne laser source, 632.8 nm). The surface morphology and microstructure of the particle and pellets were examined by a Phillips XL30 scanning electron microscope (SEM). The surface chemical analysis was carried out via a Thermo Scientific K-Alpha X-ray photoelectron spectrometer (XPS) using a monochromated Al-Kα X-ray source ($h\nu = 1486.6$ eV). The thermal conductivity of the pellets was measured using a thermal conductivity analyser (C-Therm TCi) at room temperature. The coefficient of thermal expansion is measured using a TA Q400 Thermomechanical Analyser (TMA) from room temperature to 900 °C under a N_2 atmosphere with a heating rate of 5 °C/min. The bulk density (ρ) was determined by measuring the weight (w) and the volume (v) of the pellet directly, where $\rho = w/v$. The theoretical density was estimated via the lattice parameters from XRD, and the molecular weight was calculated based on each molecular formula. The bulk thermal conductivity was calculated based on the porosity and the measured thermal conductivity using,

$$\kappa_0 = \frac{3}{3 - 4\varphi} \kappa, \tag{1}$$

where φ is the porosity, κ_0 is the corrected thermal conductivity for fully dense materials, and κ is the measured thermal conductivity[20]. The correction is based on the assumption that spherical pores are homogeneously distributed in the medium and the thermal conductivity for pores is infinite.

Simulation Method. The simulation is conducted based on the rigid-ion model. The simulation cell contains $6 \times 6 \times 32$ crystallographic unit cells, and thermal conductivity is calculated via the non-equilibrium MD simulation method[21]. In a simulation cell, particles such as Y^{3+} ions, Zr^{4+} ions and Dy^{3+} ions are randomly located in cation sites and O^{2-} ions are randomly located in anion sites. The starting positions of 4YSZ are initialized in a tetragonal lattice with an initial displacement, whereas DYZ has zero displacement in the initialized tetragonal lattice. The crystal structure information used for the starting positions is determined via the XRD method. The simulation process consists of an (N, P, T)-ensemble for the system to reach equilibrium and an (N, V, E)-ensemble for the calculation of thermodynamic properties. In the initial (N, P, T)-ensemble, in which the temperature, pressure and number of particles are constant, the atoms reach equilibrium during a period of $5 \times 10^4 - 10 \times 10^4$ time steps (25–50 ps). In the (N, V, E)-ensemble, which is referred to as the system with a constant volume, constant energy and constant number of particles, a temperature perturbation is generated within the simulation cell along the long dimension of the simulation cell during a period of 2.5×10^5 time steps

Species	A (eV)	ρ (Å)	C (eV·Å⁶)	Ref
Y^{3+}-O^{2-}	1366.35	0.348	19.6	[22]
Zr^{4+}-O^{2-}	1502.11	0.345	5.1	[22]
O^{2-}-O^{2-}	9547.96	0.224	32	[22]
Dy^{3+}-O^{2-}	1807.84	0.3393	18.77	[57]

Table 1. Interatomic potential used in the simulation.
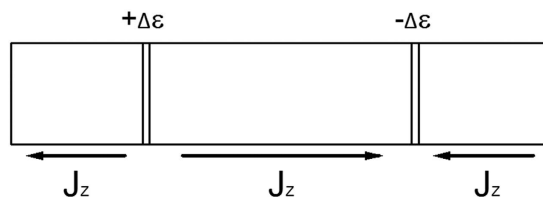
Figure 1. Diagram of the heat conduction in a periodic simulation box ($\Delta\varepsilon$ is the heat incorporated and removed from two slabs).

(125 ps). The potential is determined via Buckingham potential for the short-range interaction between ions and the long-range Coulomb interaction.

$$V_{ij} = A_{ij} \exp\left(\frac{-r_{ij}}{\rho_{ij}}\right) - \frac{C_{ij}}{r_{ij}^6} + \frac{Q_i Q_j}{4\pi\varepsilon_0 r_{ij}},$$

(2)

where A_{ij}, ρ_{ij} and C_{ij} are Buckingham potential parameters which consist of the Born-Mayer potential, $A_{ij} \exp\left(\frac{-r_{ij}}{\rho_{ij}}\right)$ and a van der Waals potential, $\frac{C_{ij}}{r_{ij}^6}$. A_{ij} indicates the repulsion between two ions when their electronic clouds overlap. ρ_{ij} is the ionic radii of two ions, and C_{ij} represents the strength of the van der Waals interaction of two ions. Q_i, Q_j and r_{ij} describe the Coulomb interaction. Q_i and Q_j are the charges of two ions, r_{ij} is the separation of two ions and ε_0 is the vacuum permittivity[22,23]. Short-range forces are calculated via the direct summation in which a cut-off radius is applied, and a long-range correction is added. The long-range forces are determined via the Wolf method[24,25]. The temperature and the pressure in the (N, P, T)-ensemble are controlled by the Berendsen barostat method and the Anderson thermostat method[26,27]. The potential parameters that have been used in the simulation are presented in Table 1.

In the non-equilibrium MD model, the heat is incorporated into a slab of materials and removed from another slab of materials, as shown in Fig. 1. The velocity-rescaling method is applied to the particles within heated and cooled slabs in the (N, V, E)-ensemble, resulting in a net kinetic energy difference of $\Delta\varepsilon$[22]. The heat current of the periodic simulation cell can be determined by,

$$J_z = \frac{\Delta\varepsilon}{2A\Delta t},$$

(3)

where $\Delta\varepsilon$ is the kinetic energy, Δt is the MD time step (0.5 fs), and A is the cross-sectional area[22]. In the MD simulation, the thermal plate power $\left(\frac{\Delta\varepsilon}{\Delta t}\right)$ is 320 nW. The simulation cell is divided into 20 slices from which the temperature gradient of the system can be determined, and the thermal conductivity is computed via Fourier's law of heat conduction,

$$J_z = -\kappa\frac{dT}{dZ},$$

(4)

where κ is the thermal conductivity, $\frac{dT}{dZ}$ is the temperature gradient along z-direction and J_z is the heat current[22].

Results and Discussion

Structural Characterization.

Scanning Electron Microscopy. The surface morphology of as-synthesized powders and pellets was characterized via SEM (Fig. 2), in order to study the influence of the microstructure on the thermodynamic properties. 4YSZ is composed of polyhedral particles with sharp edges, whereas DYZ particles exhibit more inter-particle pores. This could be due to the pyrolysis of the gel which consists of metallorganics and nitrate salts. The metallorganics tend to volatilize and combust, while nitrate salts appear to melt, forming hollow particles during combustion[28]. The formation of inter-particle pores could result in the exfoliation of small particles[29]. Moreover, the substitution concentration of ZrO_2 influences the particle sizes: higher rare earth content tends to form smaller particles due to the fact that the rare earth atoms can increase particle brittleness[30]. The cross-sectional SEM images of the morphology of the pellets [Fig. 2(c,d)] show that DYZ exhibits relatively smaller particles as compared to those of 4YSZ.
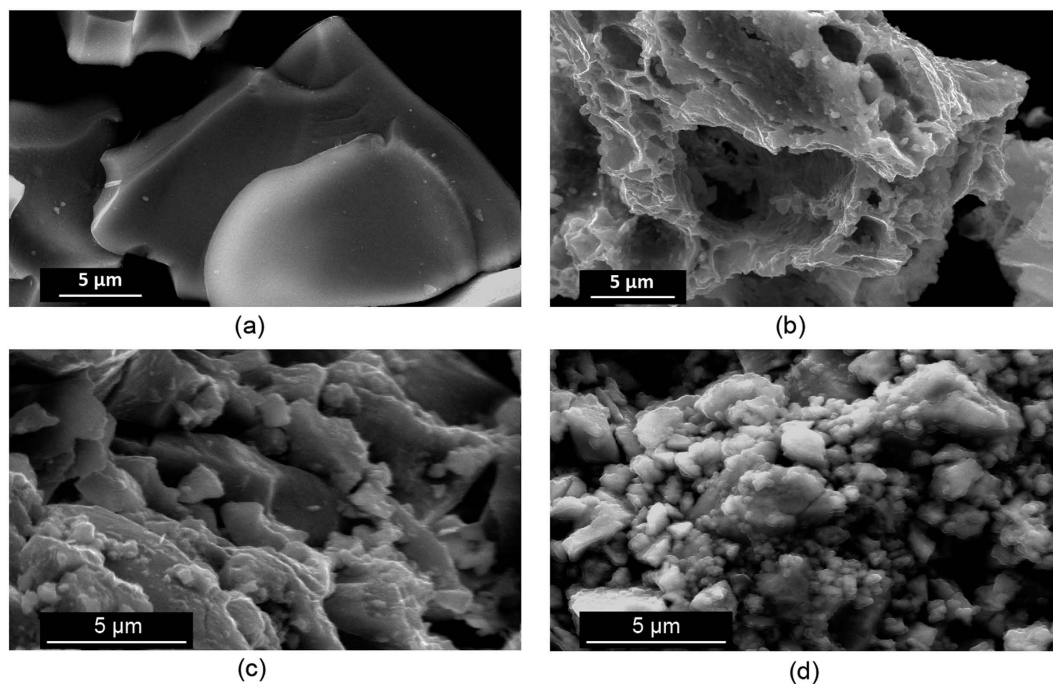
Figure 2. SEM images of: (**a**) 4YSZ particle; (**b**) DYZ particle; cross-sectional SEM images of pellets of: (**c**) 4YSZ; (**d**) DYZ.
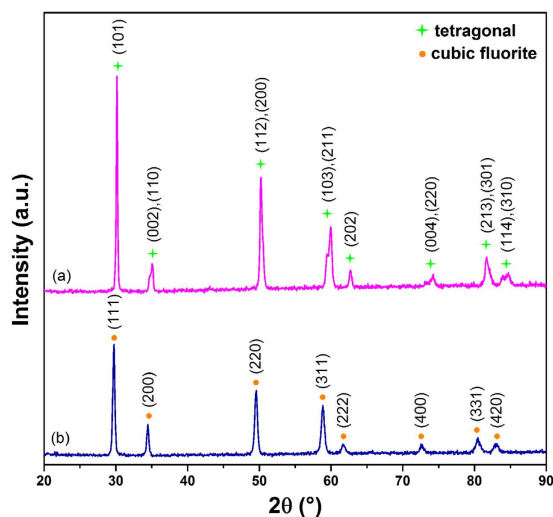
Figure 3. XRD patterns of samples sintered at 1200 °C for 2 hours for: (**a**) 4YSZ; (**b**) DYZ.

X-ray Powder Diffraction.   The phase composition was measured by XRD, as presented in Fig. 3, showing that 4YSZ consists of a tetragonal phase and DYZ consists of a cubic fluorite structure. This is confirmed from Raman analysis because both the tetragonal and cubic phases display relatively similar diffraction peaks in XRD patterns but have different vibration spectra.

The crystal size of the as-sintered powders was calculated based on line broadening using the Scherrer equation,

$$D_{XRD} = \lambda \frac{K}{B \cdot cos\,\theta},$$

(5)

where D is the dimension of crystalline, λ is the wavelength (Cu-Kα), θ is the diffraction angle, K is the constant (~ 0.9) and B is the full-width at half maximum (FWHM)[31]. The FWHM can be determined based on,

$$B_p^2(2\theta) = B_h^2(2\theta) - B_f^2(2\theta),$$

(6)

	4YSZ	DYZ
Average crystal size (nm)	22.51 ± 2.56	10.62 ± 0.78

Table 2. Average crystallite size in 4YSZ (101) plane and DYZ (111) plane after calcination at 950 °C for 3 hours.
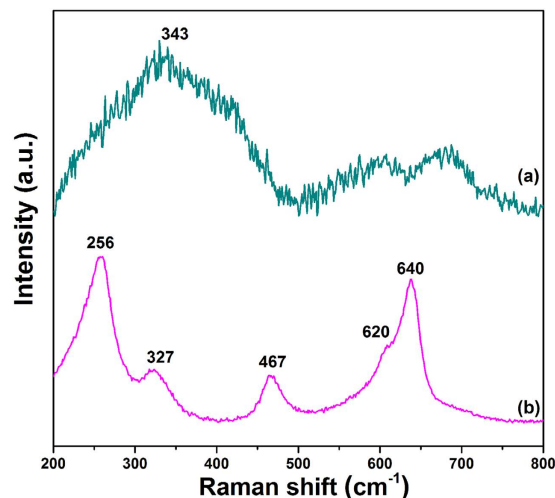
Figure 4. Raman spectra of 1200 °C sintered samples of: (**a**) DYZ (2-hour calcination); (**b**) 4YSZ (8-hour calcination).

where $B_p(2\theta)$ is the true half maximum width, $B_h(2\theta)$ is the measured half maximum width of the sample and $B_f(2\theta)$ the standard half maximum width[32]. The $\lambda_{Cu-K\alpha} = 1.5406 \times 10^{-10}$ m, and the standard material is LaB$_6$ 300. With the increase in the concentration of Dy$_2$O$_3$ and Y$_2$O$_3$, the average crystallite size decreases (Table 2). The presence of Dy^{3+} and Y^{3+} limits the grain growth of the powders.

Raman Analysis. The molecular symmetry was studied by Raman spectroscopy in order to determine the crystal structure due to the similar XRD peaks between the tetragonal structure and cubic structure, as presented in Fig. 4. In the Raman spectrum of 4YSZ, there are five active modes between 200 cm^{-1} and 800 cm^{-1}. 256 cm^{-1} is the E$_g$ stretching mode; 327 cm^{-1} indicates Zr-O B$_{1g}$ bending mode; 467 cm^{-1} is Zr-O stretching E$_g$ mode; 620 cm^{-1} is symmetric O-Zr-O A$_{1g}$ stretching mode; and 640 cm^{-1} is asymmetric O-Zr-O E$_g$ stretching mode[33]. The DYZ sample exhibits a broad-band Raman peak at 343 cm^{-1} which corresponds to the T$_{2g}$ active mode, implying a defect fluorite structure[34].

Thermochemical Compatibility. The thermochemical compatibility between Al$_2$O$_3$ and DYZ was studied via a solid-state reaction route in order to assess the high-temperature stability of DYZ to be used as a TBC material. The XRD patterns of 1300–1350 °C sintered mixed powders are shown in Fig. 5, implying that DYZ has thermochemical compatibility with Al$_2$O$_3$ up to 1300 °C. New diffraction peaks of a minor amount of Al$_5$Y$_3$O$_{12}$ and Dy$_3$Al$_5$O$_{12}$ are observed in the XRD pattern of 1350 °C sintered powder mixtures, suggesting that a solid-state reaction occurred at 1350 °C.

The morphology of DYZ and Al$_2$O$_3$ powder mixtures before and after calcination was investigated using SEM, as depicted in Fig. 6. The DYZ and Al$_2$O$_3$ powder mixtures exhibit two morphologies, including Al$_2$O$_3$ with laminar structure and DYZ with polyhedral morphology. After calcination at 1350 °C, smaller DYZ particles are deposited on the surface of Al$_2$O$_3$, probably due to the reaction.

The reaction between Al$_2$O$_3$ and DYZ can be a result of the higher driving forces of the inter-diffusion of Dy^{3+} cations into Al$_2$O$_3$ crystals when the concentration of Dy^{3+} cations and Y^{3+} cations was 25 mol %, respectively. This process can be considered as a solid-state reaction which depends on the diffusion of Al^{3+}, Dy^{3+} and Y^{3+}, controlled by a parabolic rate law,

$$\frac{dx}{dt} = k \cdot x^{-1}, \tag{7}$$

where x is the amount of reaction, t is time and k is the rate constant[35]. When the concentration of Dy^{3+} is high or the temperature of the reaction is increased, the reaction is more likely to occur.

XPS measurements were conducted to investigate the local chemical environment and the binding energy of oxygen in Al$_2$O$_3$-DYZ powder mixtures after the calcination at 1300 °C and 1350 °C (Fig. 7). There are two O1s peaks at 532.77 eV and 531.77 eV after calcination at 1300 °C. The double peaks in Fig. 7(a) could represent the O1s peak in DYZ and the O1s peak in Al$_2$O$_3$ due to the fact that the local chemical environment of the oxygen in DYZ and Al$_2$O$_3$ is different[36]. However, after the calcination at 1350 °C, the double peaks become one broad
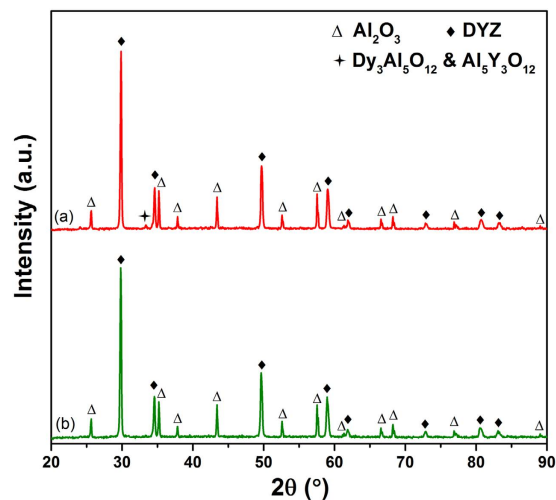
Figure 5. XRD patterns of DYZ-Al$_2$O$_3$ powder mixtures: (**a**) calcined at 1350 °C for 6 hours; (**b**) calcined at 1300 °C for 6 hours.
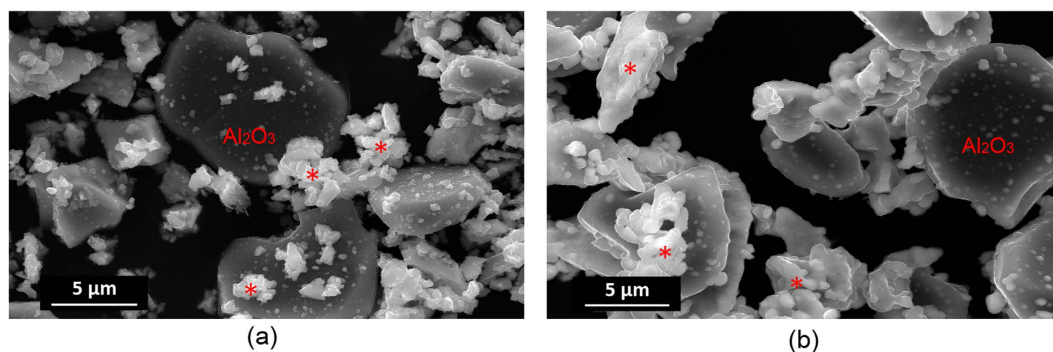
Figure 6. SEM images of powder mixtures: (**a**) ball milled DYZ and Al$_2$O$_3$ mixture; (**b**) DYZ and Al$_2$O$_3$ mixture sintered at 1350 °C for 6 hours (*represents DYZ particles).

peak at 531.65 eV, which could be explained by the improved similarity of the local chemical environment in the 1350 °C sintered Al$_2$O$_3$-DYZ powder mixture. A low-intensity O1s peak at 529.65 eV appears, probably resulting from the carbon-oxygen compound that is absorbed on the sample surface[37]. Moreover, this low-intensity O1s peak could also be due to the formation of ZrO$_2$ between Al$_2$O$_3$ and DYZ, which has a relatively lower binding energy for O1s at 529.9 eV[36]. This agrees well with the XRD results, which show that after sintering at 1350 °C the solid-state reaction between Al$_2$O$_3$ and DYZ occurs and new phases form when ZrO$_2$ is an additional product. The amount of new phases is low and the reaction occurs primarily at the interfaces between Al$_2$O$_3$ and DYZ, hence resulting in the change of the binding energy of the O1s peak.

Thermal Conductivity. The thermal conductivity of the pellets was measured using the TCi thermal conductivity analyser at room temperature. The porosity of the sintered pellets was determined using the density equation,

$$\varphi = \frac{\frac{m}{\rho_1} - \frac{m}{\rho_t}}{\frac{m}{\rho_1}} = 1 - \frac{\rho_1}{\rho_t},$$

(8)

where φ is the porosity, m is the mass of the sample, ρ_1 is the measured density and ρ_t is the theoretical density. The bulk thermal conductivity is modified considering the presence of pores within the sintered bulk pellets. These pores can scatter phonons and reduce the mean free path of these phonons, so to determine the intrinsic thermal conductivity, fully dense thermal conductivity needs to be calculated based on equation (1). The specific heat can be derived from,

$$e = \sqrt{\kappa \cdot \rho \cdot C},$$

(9)
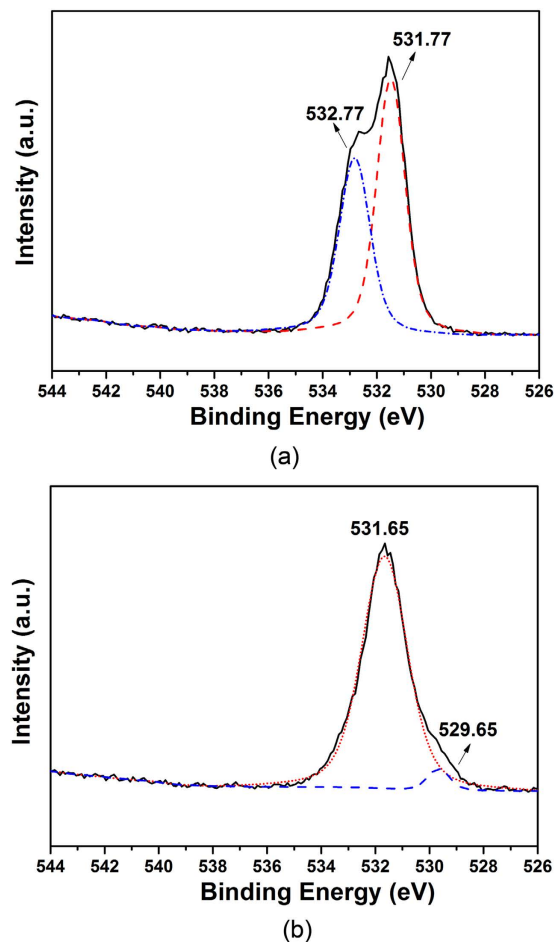
Figure 7. XPS spectra of O1s peaks of Al_2O_3-DYZ powder mixtures with 6-hour calcination at: (**a**) 1300 °C; (**b**) 1350 °C.

where e is the effusivity, κ is the thermal conductivity, ρ is the density and C is the specific heat capacity[38]. The bulk modulus is determined by,

$$\alpha = \frac{\gamma C_V}{3VB_m} = \frac{\gamma \rho C_P}{3B_m}, \tag{10}$$

where C_V is the molar isochoric heat capacity, V is the molar volume, C_P is the isobaric heat capacity, ρ is the density, B_m is the bulk modulus, α is the coefficient of thermal expansion and γ is the Grüneisen constant[39]. The coefficient of thermal expansion at 900 °C is used for the calculation of the bulk modulus from equation (10). The Young's modulus is calculated via,

$$E = 3B_m(1 - 2\nu), \tag{11}$$

where E is the Young's modulus, ν is the Poisson's ratio and B_m is the bulk modulus[40]. The minimum thermal conductivity can be calculated by,

$$\kappa_{min} = 0.87 k_B N_A^{\frac{2}{3}} \frac{m^{\frac{2}{3}} \rho^{\frac{1}{6}} E^{\frac{1}{2}}}{M^{\frac{2}{3}}}, \tag{12}$$

where E is the Young's modulus, M is the molecular weight, m is the number of atoms per molecular formula, k_B is Boltzmann's constant and N_A is Avogadro's number[41].

Table 3 depicts the corrected thermal conductivity of DYZ and 4YSZ bulk samples and the minimum thermal conductivity via Clarke's model[5]. In comparison with the measured values of 4YSZ using the same instrument, the thermal conductivity of DYZ is lower. The thermal conductivity of DYZ is lower than that of $Dy_2Zr_2O_7$ which is reported by Qu *et al.*[14]. Clarke's model is based on the Debye equation and the minimum phonon mean free path is assumed to be the cube root of the volume of a molecule[5]. The mean phonon velocity is approximated to be the mean acoustic velocity, which ignores the optical phonon modes, resulting in an underestimation of the thermal conductivity.

	4YSZ	DYZ
Effusivity (W·√s/m²·K)	1410.70 ± 66.87	1047.01 ± 44.37
Specific heat (J/kg/K)	329.38 ± 7.82	422.34 ± 42.53
Thermal conductivity (W/m·K)	2.3517 ± 0.2610	1.6727 ± 0.2861
Coefficient of thermal expansion (×10⁻⁶ °C⁻¹)	12.71	13.01
Young's modulus (GPa)	131	132
Density (g/cm³)	6.0339	6.4093
κ_{min} (W/m·K)	1.1075	0.9933

Table 3. Thermal conductivity of dense pelletized powders.

	Γ_M	Γ_δ	ε	Γ
4YSZ	0.073	0.018	40	0.78
DYZ	0.58	0.11	60	7.22

Table 4. The scattering coefficient of 4YSZ and DYZ.

Higher doping content could result in enhanced mass differences and ionic radii misfit and more oxygen vacancies within the lattice; therefore the phonon scattering is stronger. The addition of Dy^{3+} and Y^{3+} into the ZrO_2 lattice creates oxygen vacancies to maintain the charge balance. Based on the defect chemistry and Kroger-Vink notation, the formation of Dy^{3+} substitution defect can be expressed as,

$$Dy_2O_3 \xrightarrow{ZrO_2} 2Dy'_{Zr} + V_O^{\cdot\cdot} + 3O_O^x, \tag{13}$$

where Dy'_{Zr} indicates Dy^{3+} cation taking the Zr^{4+} cation site with a single negative charge, $V_O^{\cdot\cdot}$ is an oxygen vacancy with double positive charges, and O_O^x represents O^{2-} anion on the oxygen site with neutral charge[42].

In ionic oxide ceramics, two types of phonon behaviour influence the thermal conductivity, namely phonon-phonon scattering and phonon-defect scattering. In the phonon-defect scattering process, the scattering coefficient (Γ) for 4YSZ and DYZ can be determined using equation (11)–(13),

$$\Gamma_M = \frac{c_{Dy}}{c_D}\left(\frac{\Delta M_{Dy}}{\overline{M}}\right)^2_{Dy} + \frac{c_Y}{c_D}\left(\frac{\Delta M_Y}{\overline{M}}\right)^2_Y + \frac{c_{Zr}}{c_D}\left(\frac{\Delta M_{Zr}}{\overline{M}}\right)^2_{Zr} + \frac{c_O}{c_D}\left(\frac{\Delta M_O}{\overline{M}}\right)^2_{Zr} + \frac{c_V}{c_D}\left(\frac{\Delta M_{O-V}}{\overline{M}}\right)^2_{O-V}, \tag{14}$$

where Γ_M is the defect scattering coefficient due to mass misfit, $\overline{M}$ is the average atomic weight in a unit cell, C_Y, C_{Dy}, C_{Zr}, C_O, C_V, and C_D are the content of Y^{3+}, Dy^{3+}, Zr^{4+}, O^{2-}, oxygen vacancy, and overall defects, ΔM_{Dy}, ΔM_Y and ΔM_{Zr} are the atomic mass differences between the average atomic weight of the cation site ($\overline{M}_{cation}$) and Dy/Y/Zr, and ΔM_O and ΔM_{O-V} are the atomic mass differences between the anion site and O^{2-}/oxygen vacancy. Specifically, $\frac{\Delta M_{O-V}}{\overline{M}}$ is equal to $\left(-\frac{\Delta M_O}{\overline{M}} - 2\right)$ due to the fact that the number of broken bonds of an oxygen vacancy is twice as high as that per atom[43].

$$\Gamma_\delta = \frac{c_{Dy}}{c_D}\left(\frac{\Delta \delta_{Dy}}{\overline{\delta}}\right)^2_{Dy} + \frac{c_Y}{c_D}\left(\frac{\Delta \delta_Y}{\overline{\delta}}\right)^2_Y + \frac{c_{Zr}}{c_D}\left(\frac{\Delta \delta_{Zr}}{\overline{\delta}}\right)^2_{Zr} + \frac{c_O}{c_D}\left(\frac{\Delta \delta_O}{\overline{\delta}}\right)^2_{Zr} + \frac{c_V}{c_D}\left(\frac{\Delta \delta_{O-V}}{\overline{\delta}}\right)^2_{O-V}, \tag{15}$$

where Γ_δ is the defect scattering coefficient due to radius misfit, $\overline{\delta}$ is the average radius in a unit cell, $\Delta\delta_{Dy}$, $\Delta\delta_Y$, and $\Delta\delta_{Zr}$ are the radius differences between the average radius of the cation site ($\overline{\delta}_{cation}$) and Dy/Y/Zr, respectively, and $\Delta\delta_O$ and $\Delta\delta_{O-V}$ are the radius differences between anion site and O^{2-}/oxygen vacancy. The effective radius of an oxygen vacancy is assumed to be zero[44].

$$\Gamma = \Gamma_M + \varepsilon \times \Gamma_\delta = \Gamma_M + \frac{2}{9}\left(6.4 \times \gamma \times \frac{1+\nu}{1-\nu}\right)^2 \times \Gamma_\delta, \tag{16}$$

where Γ is the total defect scattering coefficient, ε is the strain field factor, γ is the Grüneisen parameter and ν is Poisson's ratio[45]. The Grüneisen parameter γ for 4YSZ is 1.40[46] and the Poisson's ratio for 4YSZ is 0.20[47]. The Grüneisen parameter γ for DYZ is assumed to be 1.54[45], estimated according to $La_2Zr_2O_7$, and the Poisson's ratio is 0.294[34], estimated based on $Dy_2Zr_2O_7$.

Table 4 shows the scattering coefficient for DYZ and 4YSZ, suggesting that the scattering coefficient of 4YSZ is lower than that of DYZ. The atomic weight of Dy (162.5) is much heavier than that of Y (88.906), resulting in the higher scattering of phonon in DYZ as compared with that in 4YSZ due to the fact that the mean free path of the phonon is inversely proportional to $\left(\frac{\Delta M}{M}\right)^2$[48].

Predicted Thermodynamic Properties. The thermal conductivity of DYZ and 4YSZ has been calculated via MD simulation in order to investigate the intrinsic property of the perfect lattice from room temperature to
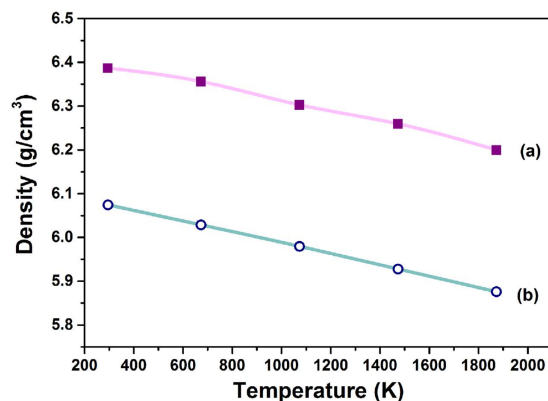
Figure 8. Predicted density of: (**a**) DYZ; (**b**) 4YSZ.

	4YSZ	DYZ
295 K	6.1408 ± 0.3634	2.4295 ± 0.1290
673 K	5.1373 ± 0.4962	2.3161 ± 0.1124
1073 K	4.8565 ± 0.6986	2.2172 ± 0.3472
1473 K	4.4404 ± 0.4010	2.0492 ± 0.3880
1873 K	4.0411 ± 0.2539	2.0531 ± 0.5538

Table 5. Predicted thermal conductivity via non-equilibrium MD simulation.

high temperatures. The reduction of thermal conductivity can be achieved by creating a novel composition such as a solid solution because dopants and the corresponding oxygen vacancies can reduce the intrinsic thermal conductivity via scattering lattice waves[49]. At 295 K, the density of 4YSZ calculated from the equilibrated crystal structure is 6.0742 g/cm^3, which agrees well with the published data of 6.0–6.1 g/cm^3 [50,51], and the calculated density of DYZ (6.3868 g/cm^3) is in strong agreement with the experimental data (6.4093 g/cm^3). Hence, the potential parameters are sufficient to generate correct lattice structure of (Dy, Y)-ZrO$_2$ in the simulation. The density of DYZ and 4YSZ from 295 K to 1874 K is presented in Fig. 8, which shows that DYZ has a relatively higher density as compared with 4YSZ. The decrease in density with the increase in temperature is due to the thermal expansion of the lattice.

The calculated thermal conductivity of DYZ and 4YSZ exhibits a decreasing trend with the increase in temperature from 295 K to 1873 K, as depicted in Table 5. This can be explained by the Umklapp phonon-phonon scattering process which dominates the heat conduction of ionic crystals at high temperature[45]. Between 295 K and 1873 K, the thermal conductivity of 4YSZ decreases by 34% which is higher than that of DYZ (11%). The influence of the Umklapp scattering process against temperature on the decrease of the thermal conductivity of 4YSZ is higher, as compared with that of DYZ. Moreover, the calculated thermal conductivity of DYZ is lower than that of 4YSZ due to the enhanced phonon-defect scattering process. The incorporation of every two Dy^{3+} cations into the ZrO$_2$ lattice creates one oxygen vacancy in order to maintain the charge neutrality. This oxygen vacancy, the mass difference, and the ionic radii difference between Dy^{3+} and Zr^{4+}, Y^{3+} and Zr^{4+} decrease the phonon mean free path and thermal conductivity[52].

The thermal conductivity of 4YSZ predicted from the simulation is higher than that measured in the experiment (2.3–3.0 W/m·K)[1,11,53,54] due to the fact that in the experiment there are defects and boundaries which can reduce the thermal conductivity. These defects and boundaries include grain boundaries, interfaces between dissimilar phases, defect clusters, micro-cracks and nano-pores[41,55,56]. The model is based on a single crystal without the influence of such defects, partly resulting in higher thermal conductivity. Moreover, as in the model reported by Schelling and Phillpot, at low temperature the relatively high thermal conductivity can be partly due to the high speed of sound in the model and the high-frequency vibrational modes which are different from the experimental work and lead to an increase of thermal conductivity[21]. This is because MD simulation is based on the assumption of Newton's equation of motion, ignoring the detail of the electronic structure of particles[17].

In addition, finite-size effects could result in the discrepancy of the thermal conductivity of DYZ and 4YSZ between the experiment and MD simulation. The thermal conductivity could be influenced by the length of the simulation cell L$_Z$, and $\frac{1}{\kappa}$ is proportional to $\left(\frac{1}{l_\infty} + \frac{4}{L_Z}\right)$ where l$_\infty$ is the phonon mean free path of an infinite system[22]. DYZ has a lower thermal conductivity, indicating that the phonon mean free path of DYZ is smaller than that of 4YSZ, especially at a lower temperature. However, the length of the simulation cell is identical for DYZ and 4YSZ, thus resulting in a larger deviation of the calculated thermal conductivity for 4YSZ than for DYZ. Moreover, it is reported by Clarke that phonons reach a minimum mean free path at high temperatures, and this is comparable with two neighbouring atoms in a lattice[5]. Thus, the thermal conductivity of DYZ and 4YSZ is more similar with each other at high temperatures than at room temperature.

Conclusions

In summary, fluorite DYZ powders and tetragonal 4YSZ powders have been synthesized via a sol-gel route. The particles exhibit polyhedral morphology with sharp edges and pores. The thermal conductivity of DYZ is lower than that of 4YSZ and the phonon-defect scattering of DYZ is stronger than that of 4YSZ. Theoretical thermal conductivity of DYZ is lower than that of 4YSZ, and the density of DYZ is higher than that of 4YSZ from 295 K to 1873 K. The influence of doping Dy^{3+} and Y^{3+} cations on the calculated thermal conductivity of ZrO_2 via MD simulation is in good agreement with the experimental measurement. At 1300 °C, there is no reaction between DYZ and Al_2O_3, whereas a minor amount of $Al_5Y_3O_{12}$ and $Dy_3Al_5O_{12}$ formed due to calcination at 1350 °C. It is discovered that DYZ exhibits lower thermal conductivity and has the potential to be used up to 1300 °C as a new ceramic TBC material.

References

1. Padture, N. P., Gell, M. & Jordan, E. H. Thermal barrier coatings for gas-turbine engine applications. *Science* **296,** 280–284 (2002).
2. Clarke, D. R. & Levi, C. G. Materials design for the next generation thermal barrier coatings. *Annu. Rev. Mater. Res.* **33,** 383–417 (2003).
3. Stöver, D. & Funke, C. Directions of the development of thermal barrier coatings in energy applications. *J. Mater. Process. Technol.* **92–93,** 195–202 (1999).
4. Bansal, N. P., Zhu, D. & Eslamloo-Grami, M. Thermal properties of oxides with magnetoplumbite structure for advanced thermal barrier coatings. *Surf. Coat. Technol.* **202,** 2698–2703 (2008).
5. Clarke, D. R. Materials selection guidelines for low thermal conductivity thermal barrier coatings. *Surf. Coat. Technol.* **163–164,** 67–74 (2003).
6. Vassen, R., Cao, X., Tietz, F., Basu, D. & Stover, D. Zirconates as new materials for thermal barrier coatings. *J. Am. Ceram. Soc.* **83,** 2023–2028 (2000).
7. Ren, X., Wan, C., Zhao, M., Yang, J. & Pan, W. Mechanical and thermal properties of fine-grained quasi-eutectoid $(La_{1-x}Yb_x)_2Zr_2O_7$ ceramics. *J. Eur. Ceram. Soc.* **35,** 3145–3154 (2015).
8. Zhou, X. *et al.* $Y_4Al_2O_9$ ceramics as a novel thermal barrier coating materials for high-temperature applications. *Mater. Lett.* **134,** 146–148 (2014).
9. Cao, X., Vassen, R. & Stoever, D. Ceramic materials for thermal barrier coatings. *J. Eur. Ceram. Soc.* **24,** 1–10 (2004).
10. Cao, X. *et al.* Lanthanum-cerium oxide as a thermal-barrier-coating material for high-temperature applications. *Adv. Mater.* **15,** 1438–1442 (2003).
11. Lu, H., Wang, C.-A. & Zhang, C. Influence of Ln^{3+} and B^{3+} ions so-substitution on thermophysical properties of $LnMB_{11}O_{19}$-type magnetoplumbite $LaMgAl_{11}O_{19}$ for advanced thermal barrier coatings. *J. Am. Ceram. Soc.* **96,** 1063–1066 (2013).
12. Guo, L., Zhang, Y. & Ye, F. Phase structure evolution and thermo-physical properties of nonstoichiometry $Nd_{2-x}Zr_{2+x}O_{7+x/2}$ pyrochlore ceramics. *J. Am. Ceram. Soc.* **98,** 1013–1018 (2015).
13. Wang, Y. J. Thermal conductivity and sintering characterists of plasma sprayed dysprosia-yttria-zirconia barrier coatings. In *Applied Science* (ed^(eds). The University of British Columbia (Vancouver) (2009).
14. Qu, L. & Choy, K.-L. Thermophysical and thermochemical properties of new thermal barrier materials based on Dy_2O_3-Y_2O_3 co-doped zirconia. *Ceram. Int.* **40,** 11593–11599 (2014).
15. Schelling, P. K., Phillpot, S. R. & Grimes, R. W. Optimum pyrochlore compositions for low thermal conductivity. *Philos. Mag. Lett.* **84,** 127–137 (2004).
16. McGaughey, A. J. H. & Kaviany, M. Thermal conductivity decomposition and analysis using molecular dynamics simulations. Part I. Lennard-Jones argon. *Int. J. Heat Mass Transfer* **47,** 1783–1798 (2004).
17. Scheerschmidt, K. Empirical molecular dynamics: possibilities, requirements, and limitations. In *Theory of Defects in Semiconductors* (ed^(eds Drabold, D. A. & Estreicher, S. K.) (2007).
18. Lau, K. C. & Dunlap, B. I. The roles of classical molecular dynamics simulation in solid oxide fuel cells. In *Molecular dynamics-theoretical developments and applications in nanotechnology and energy* (ed^(eds Wang, L.). InTech (2012).
19. Shiomi, J. Nonequilibrium molecular dynamics methods for lattice heat conduction calculations. *Ann. Rev. Heat Transfer* **17,** 177–203 (2014).
20. Schlichting, K. W., Padture, N. P. & Klemens, P. G. Thermal conductivity of dense and porous yttria-stabilized zirconia. *J. Mater. Sci.* **36,** 3003–3010 (2001).
21. Schelling, P. K. & Phillpot, S. R. Mechanism of thermal transport in zirconia and yttria-stabilized zirconia by molecular dynamics simulation. *J. Am. Ceram. Soc.* **84,** 2997–3007 (2001).
22. Schelling, P. K., Phillpot, S. R. & Keblinski, P. Comparison of atomic-level simulation methods for computing thermal conductivity. *Phys. Rev. B: Condens. Matter* **65,** 1–6 (2001).
23. Nino, J. C. *Optimization of oxide compounds for advanced inert matrix materials.* (ed^(eds). University of Florida (2009).
24. Wolf, D., Keblinski, P., Phillpot, S. R. & Eggebrecht, J. Exact method for the simulation of Coulombic systems by spherically truncated, pairwise r^{-1} summation. *J. Chem. Phys.* **110,** 8254–8282 (1999).
25. Fennell, C. J. & Gezelter, J. D. Is the Ewald summation still necessary? Pairwise alternatives to the accepted standard for long-range electrostatics. *J. Chem. Phys.* **124,** 1–12 (2006).
26. Andersen, H. C. Molecular dynamics simulations at constant pressure and/or temperature. *J. Chem. Phys.* **72,** 2384–2393 (1980).
27. Berendsen, H. J. C., Postma, J. P. M., Gunsteren, W. F. v., DiNola, A. & Haak, J. R. Molecular dynamics with coupling to an external bath. *J. Chem. Phys.* **81,** 3684–3690 (1984).
28. Hinklin, T. *et al.* Liquid-feed flame spray pyrolysis of metalloorganic and inorganic aluminia sources in the production of nanoalumina powders. *Chem. Mater.* **16,** 21–30 (2004).
29. Díaz-Parralejo, A., Macías-García, A., Sánchez-González, J., Díaz-Díez, M. Á. & Cuerda-Correa, E. M. A novel strategy for the preparation of yttria-stabilized zirconia powders: Deposition and scratching of thin films obtained by the sol–gel method. *J. Non-Cryst. Solids* **357,** 1090–1095 (2011).
30. Fenech, J., Dalbin, M., Barnabe, A., Bonino, J. P. & Ansart, F. Sol-gel processing and characterization of (RE-Y)-zirconia powders for thermal barrier coatings. *Powder Technol.* **208,** 480–487 (2011).
31. Farhikhteh, S., Maghsoudipour, A. & Raissi, B. Synthesis of nanocrystalline YSZ (ZrO_2–$8Y_2O_3$) powder by polymerized complex method. *J. Alloys Compd.* **491,** 402–405 (2010).
32. Wang, L. *et al.* A novel structure design towards extremely low thermal conductivity for thermal barrier coatings – Experimental and mathematical study. *Mater. Des.* **35,** 505–517 (2012).
33. Heiroth, S. *et al.* Crystallization and grain growth characteristics of yttria-stabilized zirconia thin films grown by pulsed laser deposition. *Solid State Ionics* **191,** 12–23 (2011).
34. Shimamura, K., Arima, T., Idemitsu, K. & Inagaki, Y. Thermophysical properties of rare-earth-stabilized zirconia and zirconate pyrochlores as surrogates for actinide-doped zirconia. *Int. J. Thermophys.* **28,** 1074–1084 (2007).
35. West, A. R. *Solid state chemistry and its applications.* John Wiley & Sons Ltd. (1985).
36. Barr, T. L. An ESCA study of the termination of the passivation of elemental metals. *J. Phys. Chem.* **82,** 1801–1810 (1978).

37. Nylund, A. & Olefjord, I. Surface analysis of oxidized aluminium. *Surf. Interface Anal.* **21,** 283–289 (1994).
38. Mikulić, D. & Milovanović, B. TCi system for non-destructive determination the thermal properties of materials. In: *10th European Conference on Non-Destructive Testing* (ed^(eds) (2010).
39. Hayashi, H. *et al.* Thermal expansion coefficient of yttria stabilized zirconia for various yttria contents. *Solid State Ionics* **17,** 613–619 (2005).
40. Wang, X. *et al.* Mechanical properties and damage tolerance of bulk $Yb_3Al_5O_{12}$ ceramic. *J. Mater. Sci. Technol.* **31,** 369–374 (2015).
41. Limarga, A. M., Shian, S., Leckie, R. M., Levi, C. G. & Clarke, D. R. Thermal conductivity of single- and multi-phase composition in the ZrO_2-Y_2O_3-Ta_2O_5 system. *J. Eur. Ceram. Soc.* **34,** 3085–3094 (2014).
42. Qiang, X. *et al.* Preparation and thermophysical properties of $Dy_2Zr_2O_7$ ceramic for thermal barrier coatings. *Mater. Lett.* **59,** 2804–2807 (2005).
43. Yang, F., Zhao, X. & Xiao, P. The effects of temperature and composition on the thermal conductivities of $[(ZrO_2)_{1-x}(CeO_2)_x]_{0.92}(Y_2O_3)_{0.08}$ ($0 \leq x \leq 1$) solid solutions. *Acta Mater.* **60,** 914–922 (2012).
44. Zhao, M. & Pan, W. Effect of lattice defects on thermal conductivity of Ti-doped, Y_2O_3-stabilized ZrO_2. *Acta Mater.* **61,** 5496–5503 (2013).
45. Wan, C. L. *et al.* Effect of point defects on the thermal transport properties of $(La_xGd_{1-x})_2Zr_2O_7$: experiment and theoretical model. *Phys. Rev. B: Condens. Matter* **74,** 1–9 (2006).
46. Kisi, E. & Ma, Y. Debye temperature, anharmonic thermal motion and oxygen non-stoichiometry in yttria stabilized cubic zirconia. *J. Phys.: Condens. Matter* **10,** 3823–3832 (1998).
47. Choi, S. R., Zhu, D. & Miller, R. A. Effect of sintering on mechanical and physical properties of plasma-sprayed thermal barrier coatings. *J. Am. Ceram. Soc.* **88,** 2859–2867 (2004).
48. Klemens, P. G. Phonon scattering by oxygen vacancies in ceramics. *Physica B* **263–264,** 102–104 (1999).
49. Klemens, P. G. & Gell, M. Thermal conductivity of thermal barrier coatings. *Mater. Sci. Eng., A* **245,** 143–149 (1998).
50. Ren, X. & Pan, W. Mechanical properties of high-temperature-degraded yttria-stabilized zirconia. *Acta Mater.* **69,** 397–406 (2014).
51. Piconi, C. & Maccauro, G. Zirconia as a ceramic biomaterial. *Biomaterials* **20,** 1–25 (1999).
52. Bhandari, C. M. & Rowe, D. M. *Thermal conduction in semiconductors* (1988).
53. Wu, J. *et al.* Low-thermal-conductivity rare-earth zirconates for potential thermal-barrier-coating applications. *J. Am. Ceram. Soc.* **85,** 3031–3035 (2004).
54. Bisson, J.-F., Fournier, D., Poulain, M., Lavigne, O. & Mévrel, R. Thermal conductivity of yttria-zirconia single crystals, determined with spatially resolved infrared thermography. *J. Am. Ceram. Soc.* **83,** 1993–1998 (2000).
55. Zhu, D. M., Chen, Y. L. & Miller, R. A. Defect clustering and nano-phase structure characterization of multi-component rare earth oxide doped zirconia-yttria thermal barrier coatings. In *27th International Cocoa Beach Conference on Advanced Ceramics and Composites: A* (ed^(eds Kriven, W. M., Lin, H. T.). Amer Ceramic Soc (2003).
56. Rauf, A., Yu, Q., Jin, L. & Zhou, C. Microstructure and thermal properties of nanostructured lanthana-doped yttria-stabilized zirconia thermal barrier coatings by air plasma spraying. *Scripta Mater.* **66,** 109–112 (2012).
57. Stanek, C. R., Minervini, L. & Grimes, R. W. Nonstoichiometry in $A_2B_2O_7$ pyrochlores. *J. Am. Ceram. Soc.* **85,** 2792–2798 (2002).

Acknowledgements

Author Contributions

L.Q. performed the experiment and molecular dynamics simulation, analysed the data and prepared the draft manuscript. Prof Choy supervised the project, and provided overall guidance and research direction. Dr Wheatley built the molecular dynamics model for the calculation of material properties. All authors reviewed the manuscript.

Additional Information

Competing financial interests: The authors declare no competing financial interests.

How to cite this article: Qu, L. *et al.* An Atomistic-Scale Study for Thermal Conductivity and Thermochemical Compatibility in (DyY)Zr₂O₇ Combining an Experimental Approach with Theoretical Calculation. *Sci. Rep.* **6,** 21232; doi: 10.1038/srep21232 (2016).